Electronic Supporting Information for

Lithium-silver alloys in anode-less batteries: comparison in liquid- and solid-electrolytes

Ju-Hyeon Lee[1], Jeong Yeon Heo[1], Ji Young Kim[2], Ki Yoon Bae[2], Samick Son[2], and Ji Hoon Lee[1,*]

[1] School of Materials Science and Engineering and KNU Advanced Material Research Institute, Kyungpook National University, Daegu, 41566, Republic of Korea

[2] Advanced Battery Development Group, Hyundai Motor Company, Hwaseong-si, Gyeongi-do 16082, Republic of Korea

Corresponding Author (Prof. Ji Hoon Lee) jihoonlee@knu.ac.kr

A. Supplementary Methods

1. Materials

All the chemicals were purchased from Sigma Aldrich unless otherwise specified. Silver nanoparticles (Ag, 99%), polymeric binder (polyvinylidene difluoride; PVDF, MW=560,000 g mol^{-1}), and *N*-methyl-2-pyrrolidone (NMP) were purchased from Sigma Aldrich. The argyrodite Li_6PS_5Cl (size = 3 μm) for the solid electrolyte (SE) layers were purchased from Wellcos Corporation. Conductive carbon black (C, Super-P) and vapour-grown carbon fibre (VGCF) were procured from TIMCAL and Showa Denko, respectively. Lithium foils (Li, 150 μm) were purchased from Honjo. 1 wt% lithium niobate ($LiNbO_3$) coated $LiNi_{0.8}Co_{0.1}Mn_{0.1}O_2$ (NCM) powder was procured from L&F Co., Ltd. A mixture of ethylene carbonate (EC) and ethyl methyl carbonate (EMC) solution (v:v=1:1) containing 1.15 M lithium hexafluorophosphate ($LiPF_6$) with 5 wt% fluoroethylene carbonate (FEC) as an additive was purchased from Echem and utilized as the liquid electrolyte (LE) without any purification. A mixture of 1,3-dioxolane (DOL)/1,2-dimethoxyethane (DME) solution (v:v = 1:1) containing 1 M lithium bis(trifluoromethanesulfonyl)imide (LiTFSI) with 1 wt% lithium nitrate ($LiNO_3$) as an additive was procured from Echem and used as a control LE without any purification.

2. Electrode fabrication

The Ag/C electrodes were fabricated by homogeneously dispersing the Ag, C, and PVDF in NMP in a mass ratio of 23.25:69.75:7. The prepared slurry was cast onto a Cu-coated Ni foil (MTI Corporation, battery grade, 18 μm) with an areal loading of 0.1 mg cm^{-2} using a doctor blade and then vacuum dried at 60 ℃ for 24 h. The working electrode was punched out (12.9 Φ) and weighed using a microbalance (XPR106, readability = 2 μg, Mettler Toledo).

For the Ag/C|LE|NCM cell, NCM cathodes were prepared similarly to the Ag/C electrode preparation, except for the mass ratio in the slurry (NCM:C:PVDF=85:10:5) and the areal NCM loading (11 mg_{NCM} cm^{-2}). For the Ag/C|SE|NCM cell, a composite cathode was manually prepared by mixing NCM, SE, and LPSCl at a mass ratio of 72.5:25:2.5 using a milling machine (Pulverizett 6, Fritsch) operated at 200 rpm for 20 min. In the Ag/C|SE|NCM-based cell, the areal NCM loading was controlled to be 11 mg_{NCM} cm^{-2}.

3. Electrochemical measurements of Ag/C electrode with SE and LE

Ag/C electrode was tested with anode-less all-solid-state batteries (ASSBs) using a home-made pressurized cell (13 Φ). First, to fabricate the SE pellet, the SE powder (150 mg) was first uniaxial-pressed at 70 MPa. Then, the aforementioned Ag/C electrode was located on the SE pellet, followed by uniaxial-pressing the Ag/C|SE pellet disk at 500 MPa to transfer Ag/C composite layers onto the SE. Then, Li foil was attached on the other side of SE pellet to form the Ag/C|SE|Li pellet disk in the cell. The cell was transferred in a housing case and tightened by applying external pressure (P_{stack}) of 65 MPa. All the fabrication processes were done in an Ar-filled glove box to avoid moisture and air exposure.

Ag/C electrode was also tested with anode-less lithium-metal batteries using typical 2032-type coin cells. The aforementioned Ag/C electrode served as a working electrode while Li foil was utilized as counter and reference electrodes. 1.15 M $LiPF_6$ in EC/EMC containing 5wt% FEC was used as LE. To separate Ag/C electrode and Li foil, porous polymer membrane (Celgard2400) was used as the separator.

Electrochemical evaluation was performed using a battery cycler (WBC3000, WonAtech, Korea) and a high-resolution potentiostat/galvanostat (SP-150e, Biologic, France) in a 60 °C thermostat chamber. The areal capacity (mAh cm^{-2}) and current density (mA cm^{-2}) in this study were based only on the area of the working electrode (*i.e.*, 12.9 Φ). For the asymmetric half-cell measurement, constant current (CC) mode was used for both charging and discharging processes within designated areal capacities (*e.g.*, 2 mAh cm^{-2}). The current densities and areal capacities are provided in the individual figures for clarity. The potential cutoff in the stripping process was set to 0.15 V vs. Li^+/Li. The voltage (V) was the potential vs. Li^+/Li unless otherwise stated in this work.

4. *In situ* XRD analyses

In situ XRD analysis was performed to monitor the phase transition of the Ag/C layers at the 5A (MS-XRS, λ = 0.69265 Å) beamline of Pohang Light Source-II (PLS-II) at Pohang Accelerator Laboratory (PAL) in the Republic of Korea. The storage ring was operated in a top-up mode at an energy of 3.0 GeV and an operating current of 250 mA. A MAR 345 image plate was used to record diffraction ring patterns in the transmission mode. A single ring pattern was corrected for 10 s and the obtained ring pattern was erased for 170 s. Thus, the typical time required for an individual pattern was ~180 s. The obtained ring patterns were converted to one-dimensional XRD data (*i.e.*, 2θ versus intensity) using the GSAS-II software.

For *in situ* XRD analyses, we utilized the modified coin cells with a 3 mm hole on the outer casings and spacers as in the previous reports.[1-3] Kapton tape served as an X-ray window. For SE-based cell, the aforementioned Ag/C|SE|Li pellet was transferred and assembled into the coin-cells. Note that the P_{stack} value in the modified coin-cells was calculated to be ~0.6 MPa by using the spring constant of the wavy spring and its thickness change. The operating temperature of 60 °C was controlled by using home-made silicon heating pad equipped with thermocouple on the surface. The coin cells were galvanostatically operated using the aforementioned high-resolution potentiostat/galvanostat (SP-150e).

5. XAFS analysis at the Ag K-edge

XAFS analysis was performed to characterize the physicochemical structure of the Ag at different states of charging. XAFS measurements were conducted at the 10C beamline (Wide XAFS) of PLS-II. The storage ring was operated in a top-up mode at an energy of 3.0 GeV and an operating current of 250 mA. The XAFS spectra at the Ag K-edge were achieved under transmission mode using a double-crystal monochromator (Si(111)) detuned to 80% of its maximum intensity. Calibration of each spectrum was conducted using the edge energy (E_o) of the reference Ag foil that was recorded simultaneously.

The DEMETER package containing the ATHENA and ARTEMIS software was used for processing and analyzing the X-ray absorption near-edge structure (XANES) and extended XAFS (EXAFS) data.[4-6] The detailed processing procedures followed those in previous reports.[1-3] The XANES spectra were analyzed to characterize the oxidation state change of the Ag in the Ag/C induced by the alloying reaction with Li. The Hanning window was used to obtain the Fourier-transformed (FT) EXAFS spectra in the R space (Å).

6. Cross-sectional characterization

The cross-sectional images of the Ag/C layers at different states of charging in the LE and SE-based cells were obtained by using field emission scanning electron microscopy (FE-SEM, S-4800, Hitachi) equipped with energy dispersive spectroscopy (EDS, EX-250, Horiba) and ion-milling machine (E-3500, Hitachi).

B. Supplementary Figures

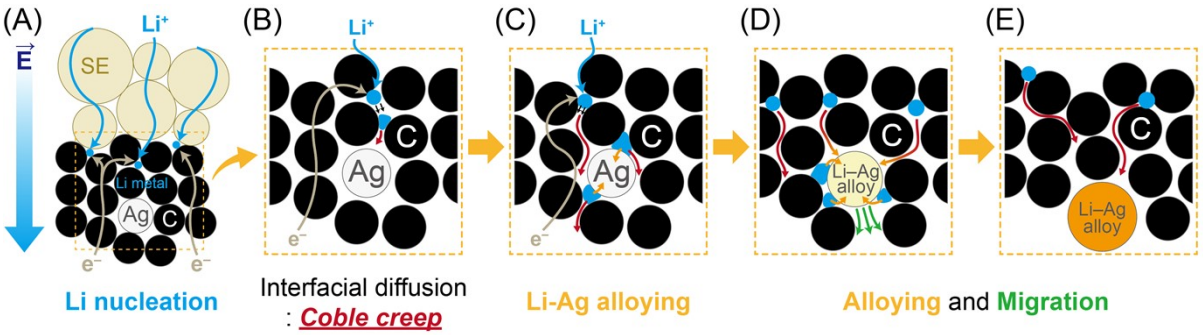

Fig. S1. Schematic of Li nucleation, diffusion (movement), and alloying processes in an SE-based cell.

[Supplementary Note on Fig. S1]

Li diffusion, Li deposition, and Li-Ag alloying processes are more complicated in SE-based cells than in LE-based cells. This complexity arises from the non-uniformity of the Ag/C|SE interfaces. This non-uniformity results in a situation in which the energetics of Li deposition and Li-Ag alloying are affected by the diffusion kinetics of Li ions passing through Ag/C layers. As highlighted in previous studies that used *in situ* TEM analyses,[7, 8] Li nucleation, controlled by the electrochemical reaction of "$Li^+ + e^- \rightarrow Li$", occurs within the Ag/C layers by filling the pores (**Fig. S1A).** These Li nucleates then move along the interfaces between SE, C, and Ag, traversing the Ag/C layers through a diffusional Coble creep process (**Fig. S1B**). Given that the Coble creep process is driven by surface diffusivity,[9] kinetic parameters such as operating temperature, operating pressure, and pore size (considered as the size of the Li nucleates) significantly influence Li movement. Furthermore, Li nucleation involving Ag particles results in Li-Ag alloys ("$yAg+x(Li^+ + e^-) \rightarrow Li_xAg_y$", **Fig. S1C**), which move towards the current collector (CC) via consecutive alloying reactions (**Fig. S1D** and **S1E**). Consequently, the sluggish Li diffusion kinetics caused by the non-uniform Ag/C|SE interface not only affects the location of the Li deposits but also influences the phase evolution of Li-Ag alloys in the SE-based cells.

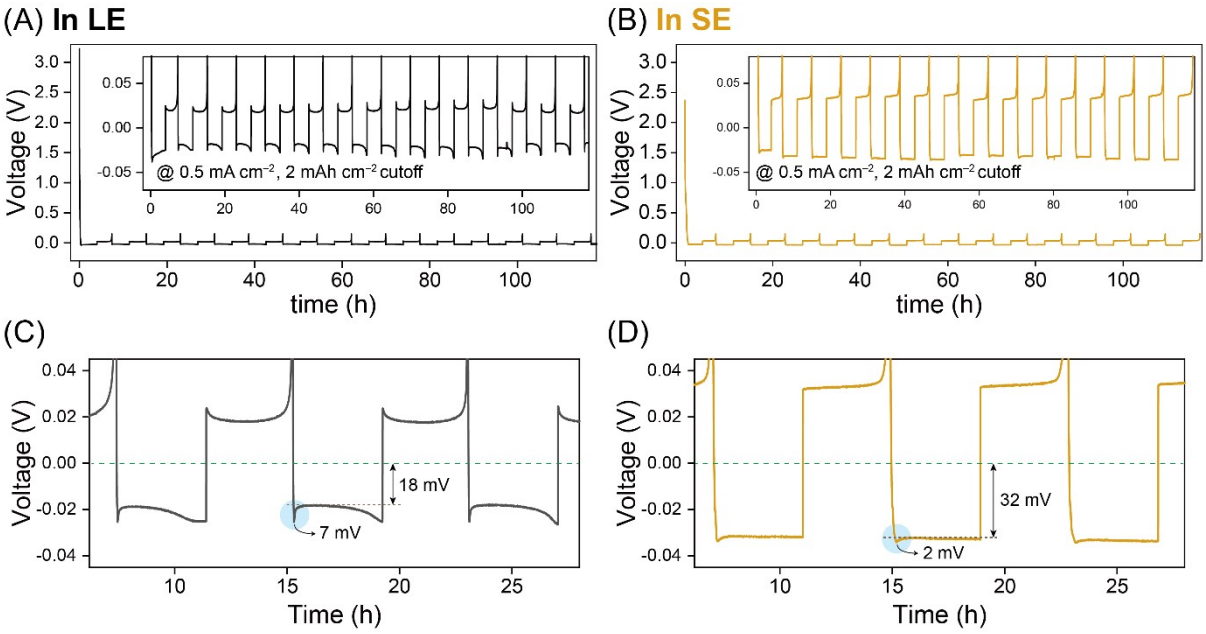

Fig. S2. Extended cycling performance of Ag/C layers in (A) LE- and (B) SE-based cells. Magnified galvanostatic plating/stripping profiles of Ag/C layers in (C) LE- and (D) SE-based cells.

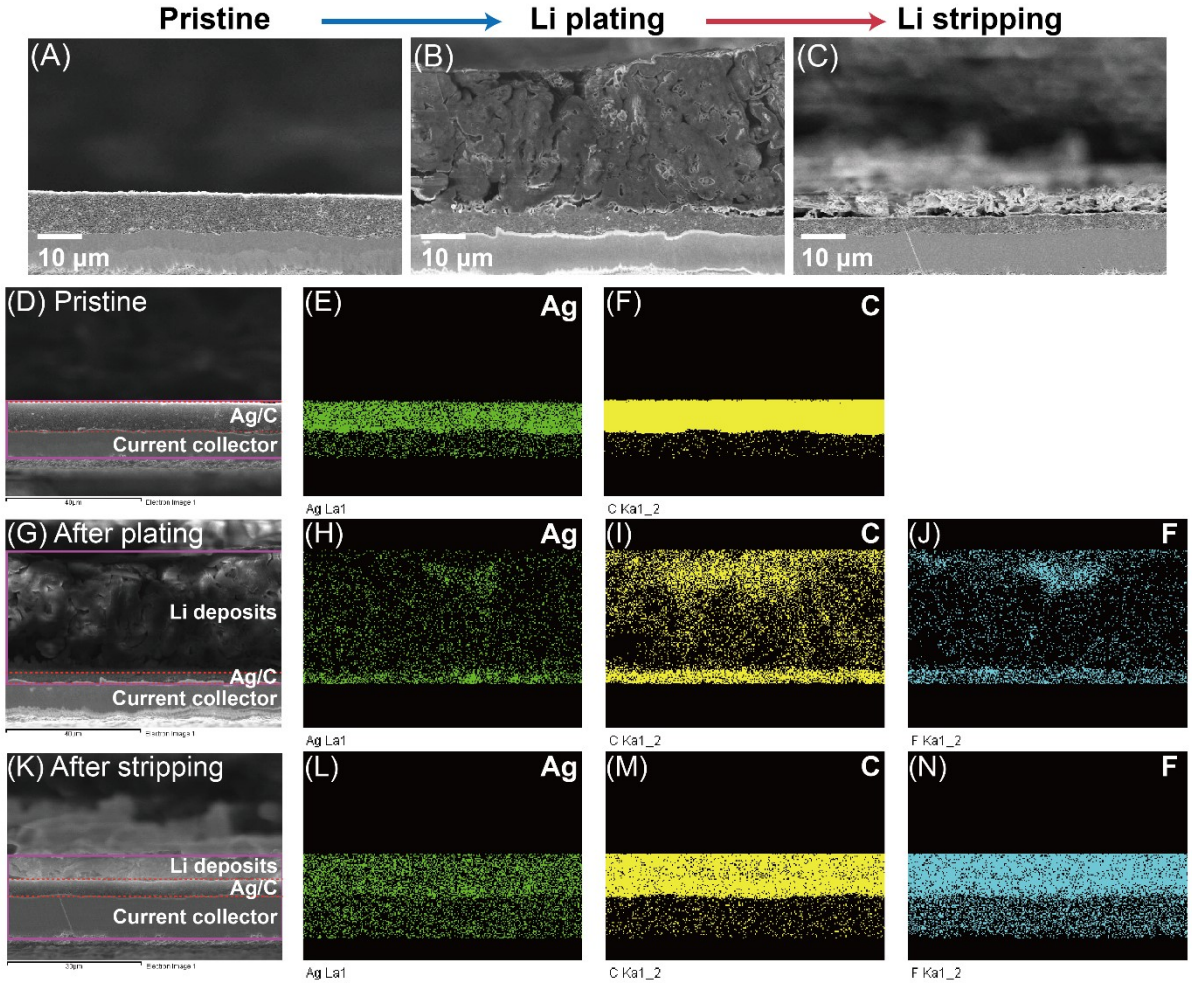

Fig. S3. Cross-sectional SEM images with the corresponding EDS mapping images of the Ag/C layers in the LE-based cells at different states of charging.

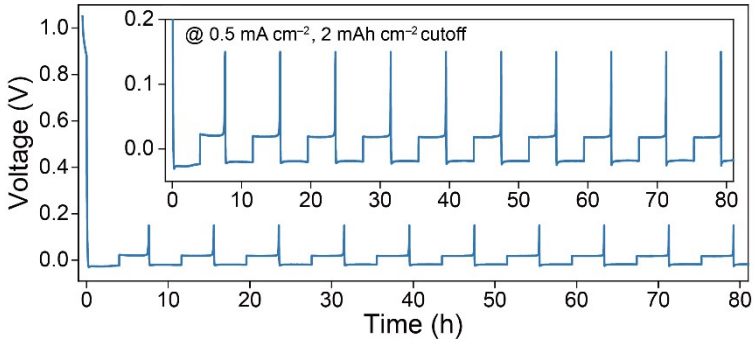

Fig. S4. Galvanostatic Li plating/stripping profiles of Ag/C layers in a LE-based cell containing 1M LiTFSI dissolved in DOL/DME with 1 wt% $LiNO_3$.

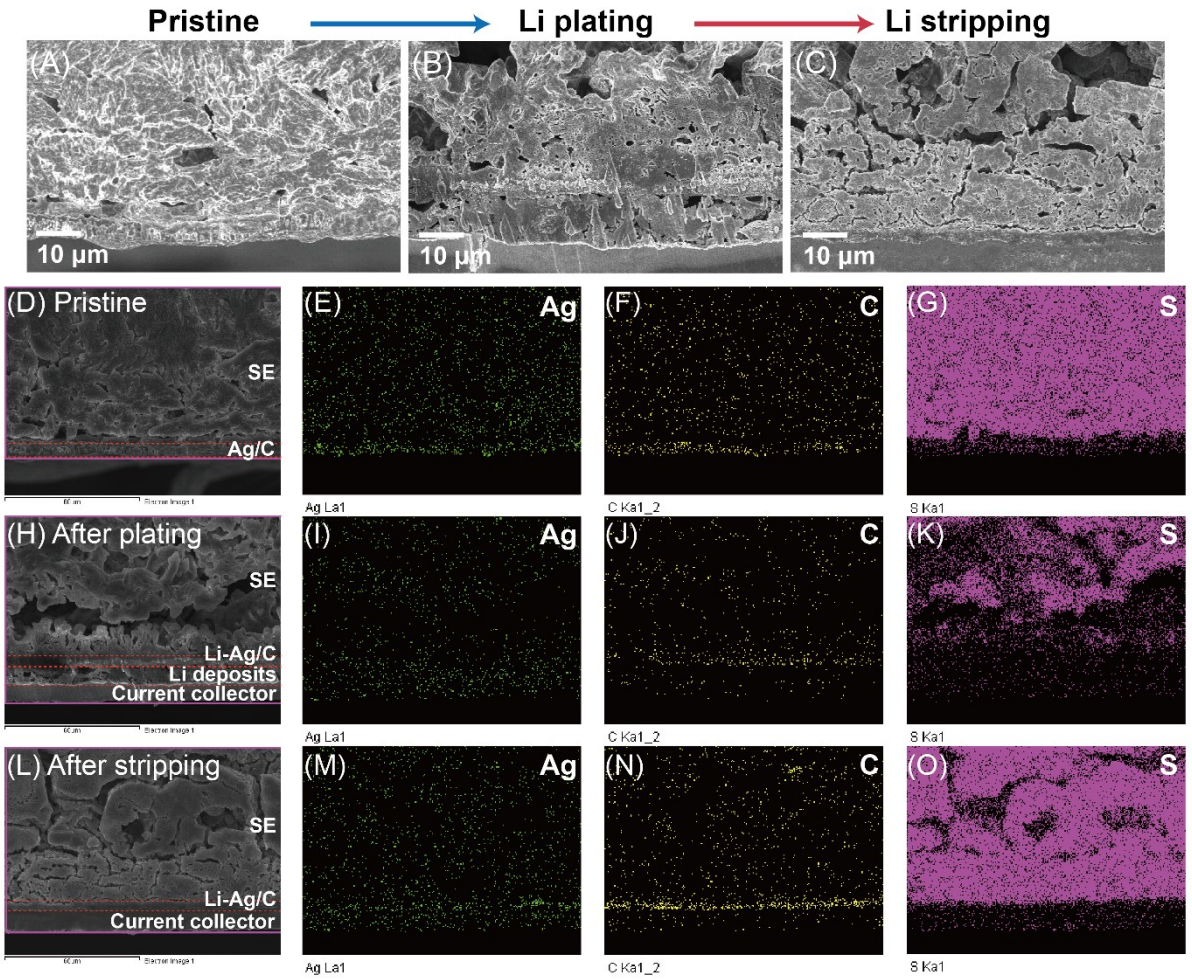

Fig. S5. Cross-sectional SEM images with the corresponding EDS mapping images of the Ag/C layers in the SE-based cells at different states of charging. Note that due to the high S concentration in the SE layers, the EDS signals for Ag and C, which have relatively low concentrations, appear scattered.

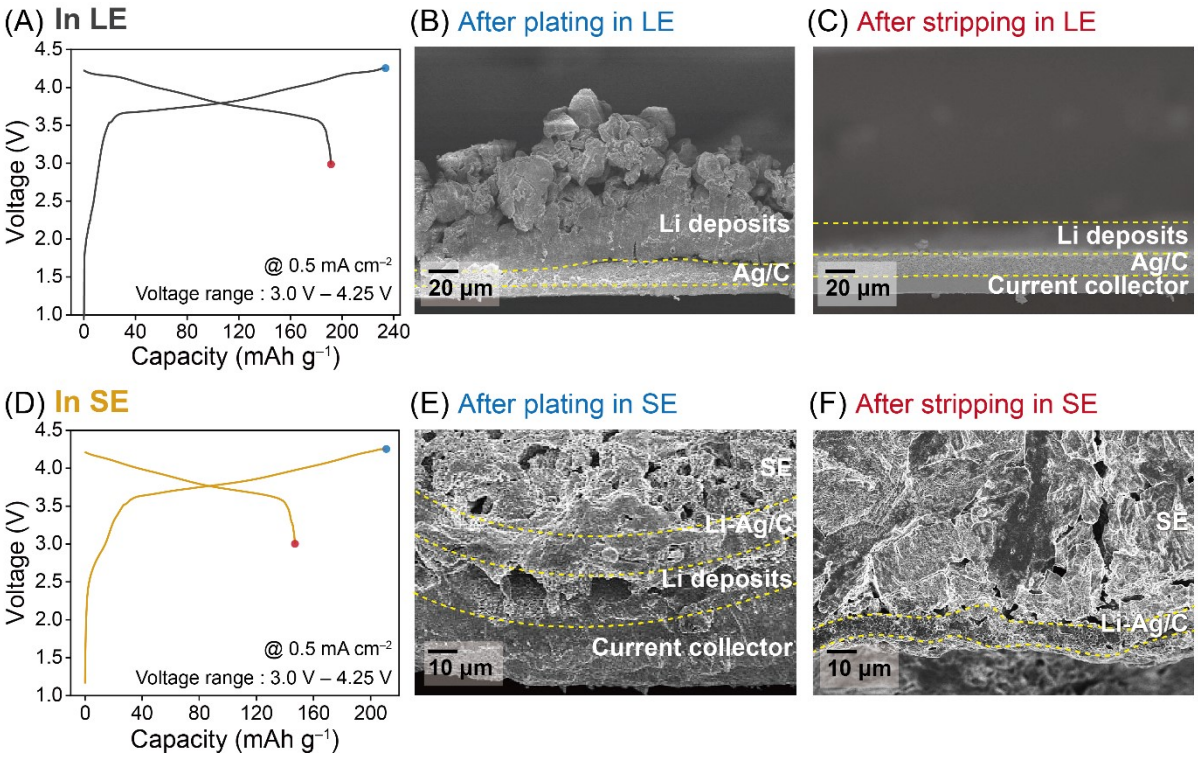

Fig. S6. Typical galvanostatic profiles and cross-sectional SEM images of Ag/C layers at different states of charging obtained from (A–C) Ag/C|LE|NCM and (D–F) Ag/C|SE|NCM cells.

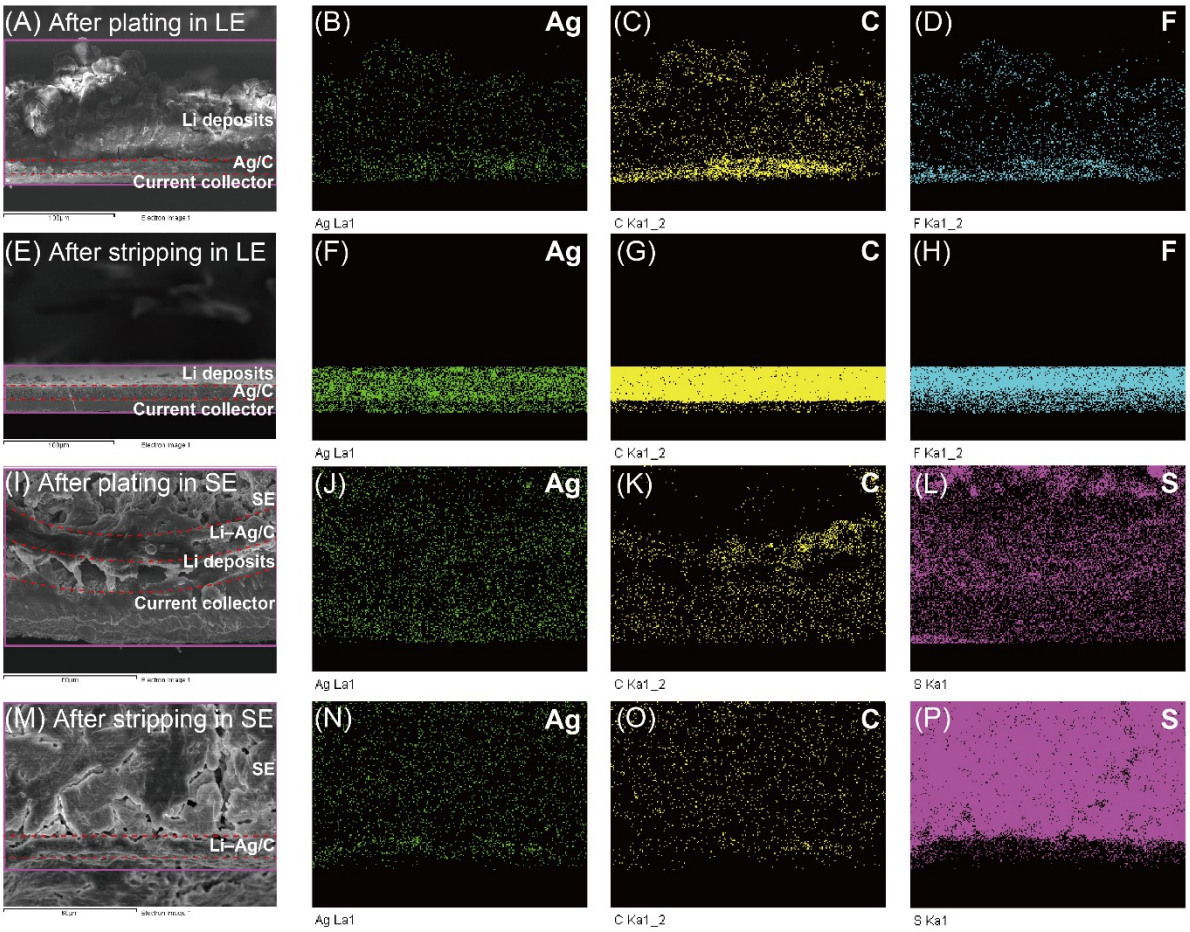

Fig. S7. Cross-sectional SEM images with corresponding EDS mapping images of the Ag/C layers obtained from (A-H) the Ag/C|LE|NCM and (I-P) the Ag/C|SE|NCM cells at different states of charging.

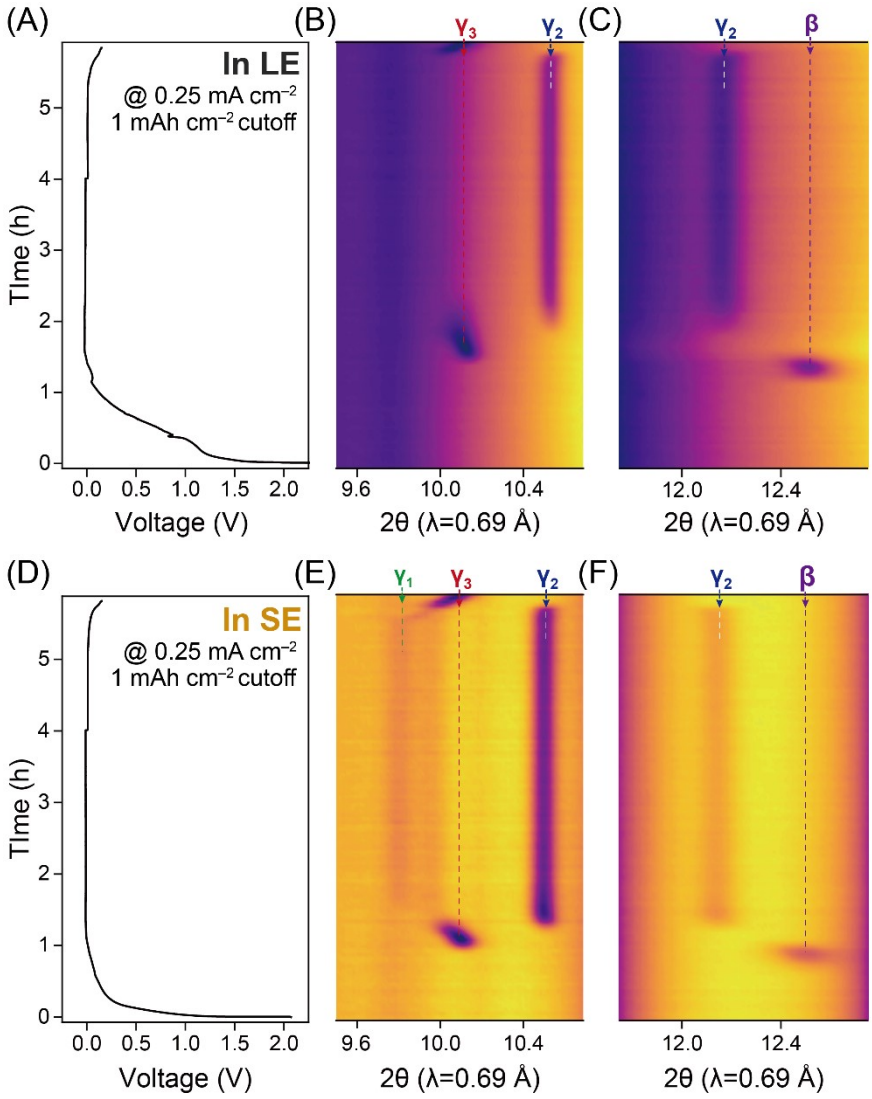

Fig. S8. Additional *in situ* XRD results of the Ag/C layers in (A-C) LE- and (D-F) SE-based cells.

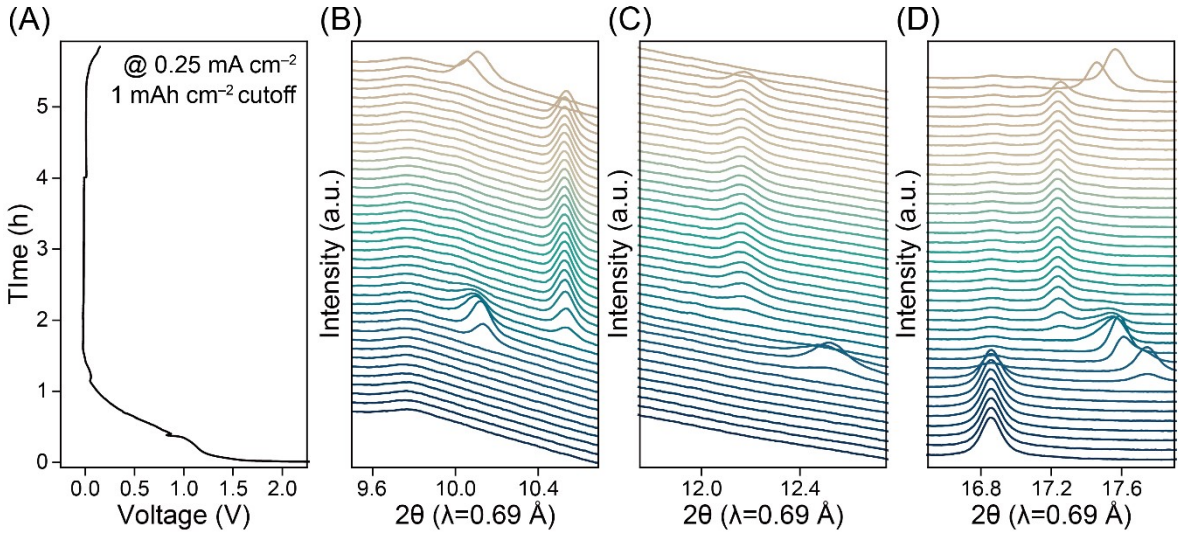

Fig. S9. XRD patterns obtained during *in situ* XRD analyses of the Ag/C layers in the LE-based cell.

Fig. S10. XRD patterns obtained during *in situ* XRD analyses of the Ag/C layers in the SE-based cell.

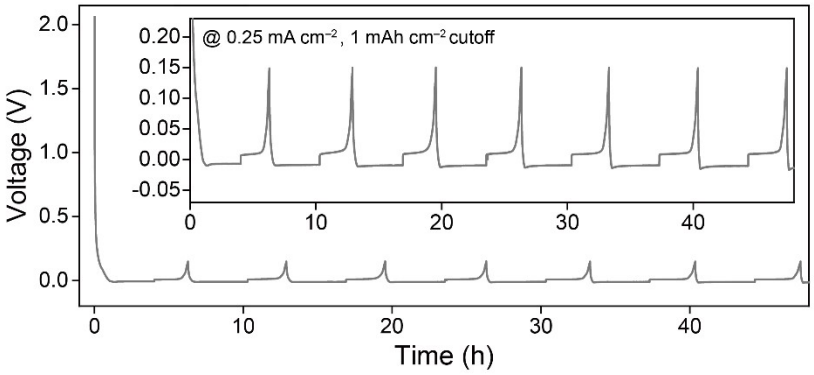

Fig. S11. Galvanostatic Li plating/stripping profiles of Ag/C layers in the SE-based coin cells.

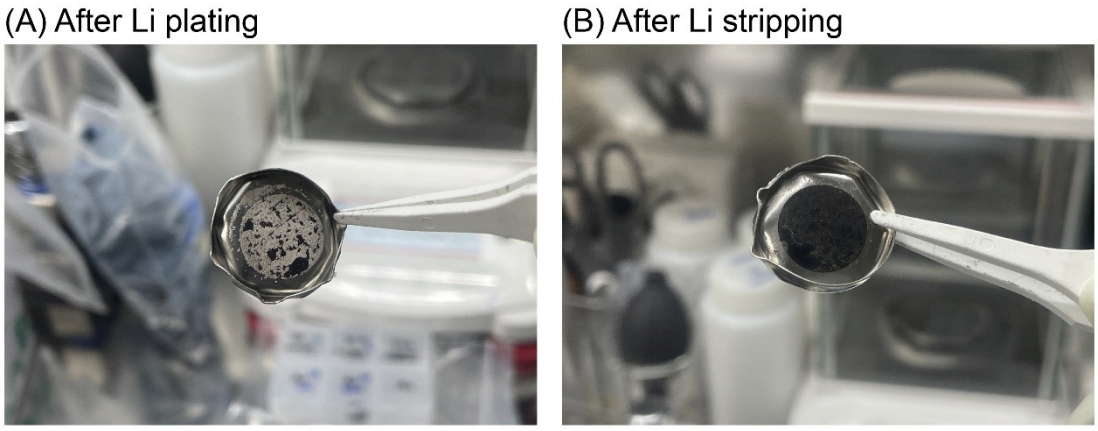

Fig. S12. Digital images of Li deposits on the Ag/C layers in the LE-based cells (A) at the Li plating of 2 mAh cm^{-2} and (B) at the Li stripping at 0.15 V. Note that the irregular location of Li deposits in (A) and the residual Li deposits in (B).

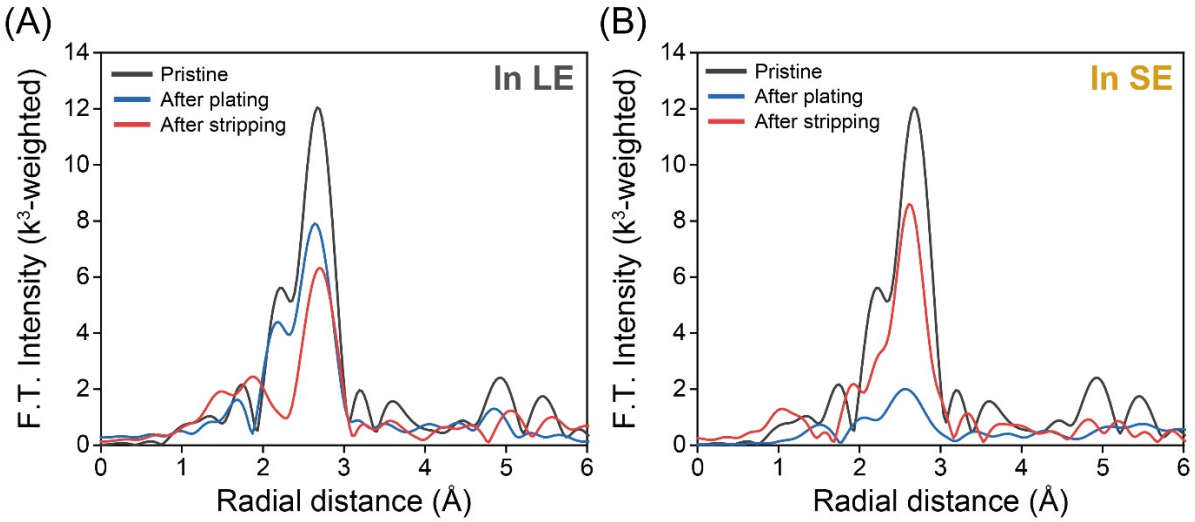

Fig. S13. Comparative EXAFS profiles of the Ag/C layers at different charging states in the (A) LE- and (B) SE-based cells.

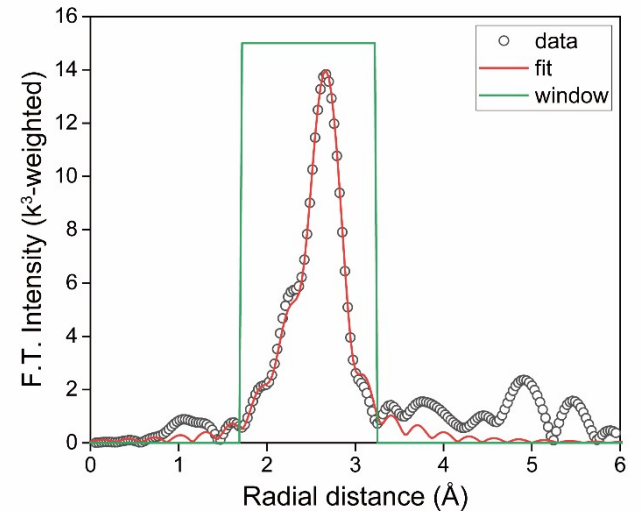

Fig. S14. EXAFS fitting result of the reference Ag foil.

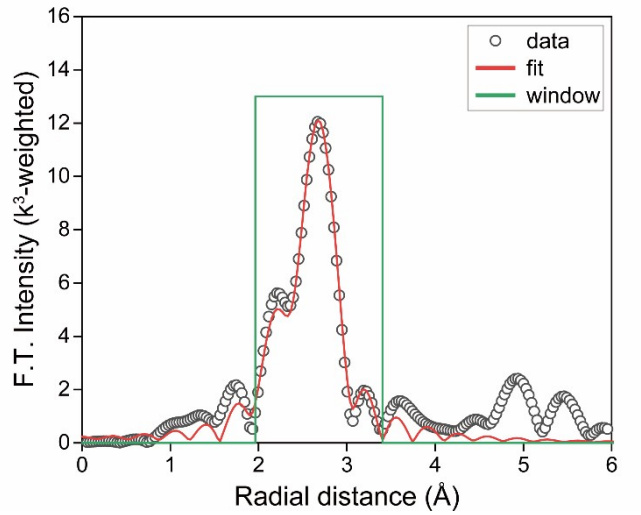

Fig. S15. EXAFS fitting result of the pristine Ag/C layers.

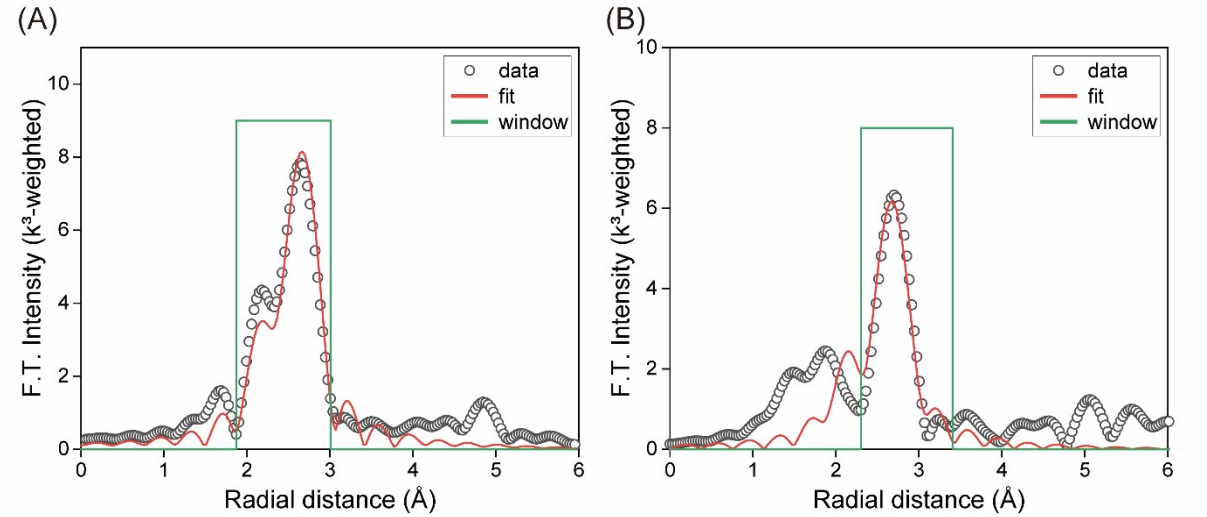

Fig. S16. EXAFS fitting results of the Ag/C layers at different charging states in the LE-based cells. (A) Li plating of 2 mAh cm^{-2} and (B) stripping at 0.15 V.

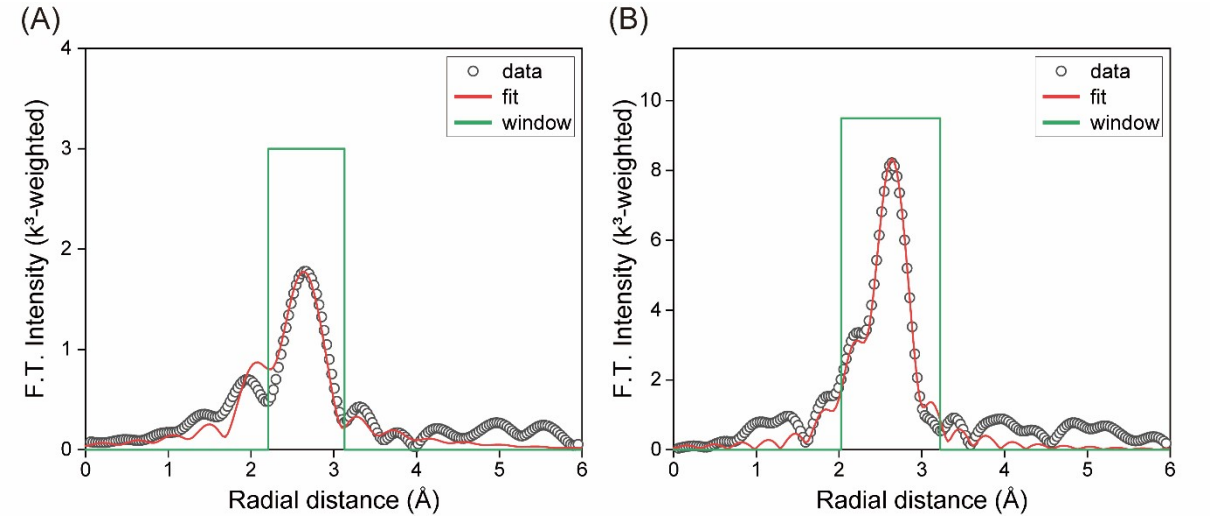

Fig. S17. EXAFS fitting results of the Ag/C layers at different charging states in the SE-based cells. (A) Li plating of 2 mAh cm^{-2} and (B) stripping at 0.15 V.

C. Supplementary Tables

Table S1. EXAFS fitting model structure.

Structure Model	
Chemical formula	Ag
Space group	$Fm\bar{3}m$
Lattice constant	4.08620 Å

Table S2. EXAFS fitting result of the reference Ag foil.

Path	Model C.N.	S_o^2 [a]	R_{model} (Å)	R_{fit} (Å)	ΔE (eV)	σ^2 ($\times 10^3$, Å^2)
Ag-Ag1	12	0.85	2.8894	2.889(2)	4.4(2)	9.5(2)
Fitting results						
Independent points	10.4316406					
Number of variables	4					
Chi-square	2979.0442444					
Reduced Chi-square	463.1857434					
R-factor	0.0023219					
Number of data sets	1					
k-range	3.000 - 13.977					
R-range	1.7 - 3.25					

[a] Amplitude reduction factor (S_o^2) obtained from this fitting was used for calculating the coordination number of Ag in the Ag/C layers.

Table S3. EXAFS fitting result of the pristine Ag/C layer.

Path	Model C.N.	Fitted C.N.	R_{model} (Å)	R_{fit} (Å)	ΔE (eV)	σ^2 ($\times 10^3$, Å^2)
Ag-Ag1	12	11.7(6)	2.8894	2.87(4)	3.5(4)	9.7(5)
Fitting results						
Independent points	8.2207031					
Number of variables	4					
Chi-square	144.8934260					
Reduced Chi-square	34.3292152					
R-factor	0.0043861					
Number of data sets	1					
k-range	3.000 - 12.217					
R-range	1.95 - 3.4					

Table S4. EXAFS fitting result of the Ag/C layer at the Li plating of 2 mAh cm^{-2} in the LE-based cell.

Path	Model C.N.	Fitted C.N.	R_{model} (Å)	R_{fit} (Å)	ΔE (eV)	σ^2 ($\times 10^3$, Å^2)
Ag-Ag1	12	7.5(8)	2.8894	2.850(7)	2.8(8)	9(1)
Fitting results						
Independent points	6.1523437					
Number of variables	4					
Chi-square	465.9438414					
Reduced Chi-square	216.4820751					
R-factor	0.0102960					
Number of data sets	1					
k-range	3.000 - 11.8					
R-range	1.87 - 3					

Table S5. EXAFS fitting result of the Ag/C layer at the stripping state of 0.15 V in the LE-based cell.

Path	Model C.N.	Fitted C.N.	R_{model} (Å)	R_{fit} (Å)	ΔE (eV)	σ^2 ($\times 10^3$, Å^2)
Ag-Ag1	12	8.1(8)	2.8894	2.856(9)	2.3(7)	12(1)
Fitting results						
Independent points	5.9814453					
Number of variables	4					
Chi-square	247.7052114					
Reduced Chi-square	125.0123886					
R-factor	0.0125604					
Number of data sets	1					
k-range	3.000 - 11.8					
R-range	2.3 - 3.4					

Table S6. EXAFS fitting result of the Ag/C layer at the Li plating of 2 mAh cm^{-2} in the SE-based cell.

Path	Model C.N.	Fitted C.N.	R_{model} (Å)	R_{fit} (Å)	ΔE (eV)	σ^2 ($\times 10^3$, $Å^2$)
Ag-Ag1	12	1.3(2)	2.8894	2.82(2)	−1(2)	6.09[a]
Fitting results						
Independent points	4.1064453					
Number of variables	3					
Chi-square	12.7105054					
Reduced Chi-square	11.4876942					
R-factor	0.0201758					
Number of data sets	1					
k-range	3.000 - 10.3					
R-range	2.2 - 3.1					

[a] This parameter was fixed as the optimal value in the final step of the fitting process to reduce the uncertainty of the coordination number for the corresponding path.

Table S7. EXAFS fitting result of the Ag/C layer at the stripping state of 0.15 V in the SE-based cell.

Path	Model C.N.	Fitted C.N.	R_{model} (Å)	R_{fit} (Å)	ΔE (eV)	σ^2 ($\times 10^3$, Å^2)
Ag-Ag1	12	7.9(5)	2.8894	2.845(5)	2.3(5)	10.0(6)
Fitting results						
Independent points	7.3847656					
Number of variables	4					
Chi-square	59.4000685					
Reduced Chi-square	17.5492412					
R-factor	0.0050974					
Number of data sets	1					
k-range	3.000 - 13					
R-range	2 - 3.2					

D. Supplementary References

1. J.-H. Lee, J.-G. Bae, M. S. Kim, J. Y. Heo, H. J. Lee and J. H. Lee, *ACS Nano*, 2024, **18**, 1995-2005.
2. J. Y. Heo, J.-H. Lee, J.-G. Bae, M. S. Kim, H. J. Lee and J. H. Lee, *Green Chem.*, 2023, **25**, 6823-6831.
3. J.-G. Bae, J.-H. Lee, M. S. Kim, B. G. Kim, H. J. Lee and J. H. Lee, *ACS Appl. Mater. Interfaces*, 2023, **15**, 7939-7948.
4. B. Ravel and M. Newville, *J. Synchrot. Radiat.*, 2005, **12**, 537-541.
5. S. D. Kelly, D. Hesterberg and B. Ravel, in *Methods of Soil Analysis Part 5—Mineralogical Methods*, 2008, DOI: 10.2136/sssabookser5.5.c14, pp. 387-463.
6. J. J. Rehr and R. C. Albers, *Rev. Mod. Phys.*, 2000, **72**, 621-654.
7. Y. Chen, Z. Wang, X. Li, X. Yao, C. Wang, Y. Li, W. Xue, D. Yu, S. Y. Kim, F. Yang, A. Kushima, G. Zhang, H. Huang, N. Wu, Y.-W. Mai, J. B. Goodenough and J. Li, *Nature*, 2020, **578**, 251-255.
8. Z. Wang, X. Li, Y. Chen, K. Pei, Y.-W. Mai, S. Zhang and J. Li, *Chem*, 2020, **6**, 2878-2892.
9. S. H. Park, D. Jun, J. E. Jung, S. G. Lee, G. H. Lee and Y. J. Lee, *J. Mater. Chem. A*, 2022, **10**, 21995-22006.